Chapter 7

Video Measurements and Analysis of Surface Gravity Waves in Shallow Water

Charles R. Bostater Jr, Bingyu Yang and Tyler Rotkiske

Additional information is available at the end of the chapter

http://dx.doi.org/10.5772/intechopen.73042

Abstract

This paper discusses a shallow-water wave height measurement method that uses high definition video cameras to image a water surface wave patch. Wave height time series are extracted from water surface video sequences. Wave features such as the wavelength distribution and energy contained in a wave patch (W/m^2) were obtained by analyzing the extracted wave height time series and expressing the wind-driven wave energy as a wave energy spectrum. A Weibull probability distribution was used as the mathematical form of the energy spectrum. Wave spectra are used as input to a wave patch simulation model that generates simulated wind-driven wave images. The measurement protocol is inexpensive, easy to implement, and useful to calibrate and validate wind-driven wave models. The protocol is used to understand resuspension of bottom muds due to wind waves in shallow waters. Scaled staff gauges made of polyvinyl chloride (PVC) materials are placed in shallow water and imaged at 30 Hz followed by frame based image analysis to extract wave height time series. Wave spectra calculated using the fast Fourier transform (FFT) results in a Weibull probability distribution function (WPDF) energy spectrum. The estimated wave spectrum is used to estimate wave energy in W/m^2 followed by generation of wave patch simulations of the water surface. Simulated wave patches are compared with the sensor-based wave patch video measurements. Sensitivity analysis of coefficients α and β in the model are used to adjust the synthetic wave images to measured wave patch images. The approach allows one to obtain an estimate of the energy (W/m^2) transferred from the local wind field to a water surface gravity wave patch.

Keywords: water surface waves, gravity waves, wind driven waves, wave patches, wave patch energy, remote sensing, staff gauges, video imaging, video analysis, energy spectra, Weibull distributions, synthetic imaging, wind energy

1. Introduction

Differential heating of the earth causes large-scale atmospheric pressure gradients. These gradients and the acceleration due to rotation of the earth result in the major wind fields around the globe. The winds cause friction on the water surface and result in the generation of wind-driven water surface gravity waves. These wind-driven gravity waves are a major source of transfer of energy from the sun and atmosphere to the earth's water system on a global scale as well as in small water regions. Measurements of these wind-driven shallow-water surface gravity wave characteristics such as wave height, period, and direction of propagation are key to understanding the magnitude of energy in a small gravity wave field or "wave patch." These surface wind-driven waves cause orbital motion of water parcels [1]. In water the wind stress or friction causes the downward movement or transport of momentum from the water surface to the water column. The downward transport of momentum causes internal friction in the water in the form of turbulent friction or viscosity, and the associated circular eddy-type motions influence the bottom lutocline within the bottom boundary layer [2, 3]. The resulting shearing forces at the bottom in shallow water cause resuspension of and fluidization of bottom sediments and associated nutrients and/or trace metals. The fluidization can result in fluidized mud, muck, high-bottom water turbidity, and nephelometric wave motions (internal wavelike motions that are observed in acoustic imaging of the bottom water column). Thus, water quality variables are influenced by the surface water wave field driven by surface winds. Bottom orbital or elliptical velocities due to these wind-driven gravity waves in shallow water can be calculated using surface wind-driven gravity wave information, such as significant wave height and wave spectra [3, 4].

Wind-driven gravity waves in water can be measured using numerous techniques and descriptions, including satellite altimeters, video cameras, wave buoys, and many types of wave gauges [5]. Altimeters flown on satellites such as Seasat in 1978, Geosat from 1985 to 1988, ERS-1 and ERS-2 from 1991, TOPEX/Poseidon from 1992, Jason from 2001, and Envisat can provide data for monthly mean maps of wave heights and the variability of wave energy density in time and space [5]. Wave height estimations based on binocular or trinocular imaging also allow acquisition of both spatial and temporal wave information for surface wave patches [6, 7, 14]. Many types of wave gauges including resistance-type, capacitance-type, and wave pressure gauges can also provide data for quantifiable wind-driven gravity wave height estimations [8]. However, there is a need to develop measurement system methods [17, 18] for shallow-water areas since most systems developed to date can only be used in deep waters (>3–5 m).

In this research, a technique or protocol that combines gravity wave staff gauges, HD video cameras [14], and image analyses is used to measure wind-driven gravity waves in shallow-water environments that receive energy from the atmosphere. Wave height time series are extracted from video sequence taken using high-definition (HD) video cameras at a 30 Hz frame rate. Significant wave height, wave spectrum, and wave energy (W m^2) are estimated from the video-based wave height time series.

In this chapter, techniques to describe the protocol are demonstrated for shallow water near the Atlantic Ocean and Space Coast Region of the Banana River estuary and watershed, near Melbourne, Florida. Simulated wave patch synthetic images are then generated using estimated wave spectrum derived from video imagery and compared to the video images.

2. Techniques and methods

2.1. Video imaging and staff gauge system

Staff gauges and HD video cameras (JVC Everio HD cameras) are used to measure the surface wave heights in shallow water (1–2 m) as shown in **Figure 1(a)**. Four staff gauges are mounted in the water by inserting them into the bottom sediment. Staff gauges are constructed from white PVC pipes. Waterproof paper with 0.5 spaced horizontal lines is taped to each gauge pipe.

Images recorded at 1920 × 1080 pixels (30 per second of recording time) obtained from the video sequence yield spatial resolution (using lens zooming) is 0.04 cm/pixel. Each line is either 1 mm (≈2 pixels) or 0.5 mm (≈1 pixel) as shown in **Figure 1(b)**. The HD cameras are mounted on a tripod on the shore or from a fixed platform or mount in the water. The video staff gauges allow one to define a wave patch of ~4.5 × 4.5 m ($W_x = W_y = 4.5$ m).

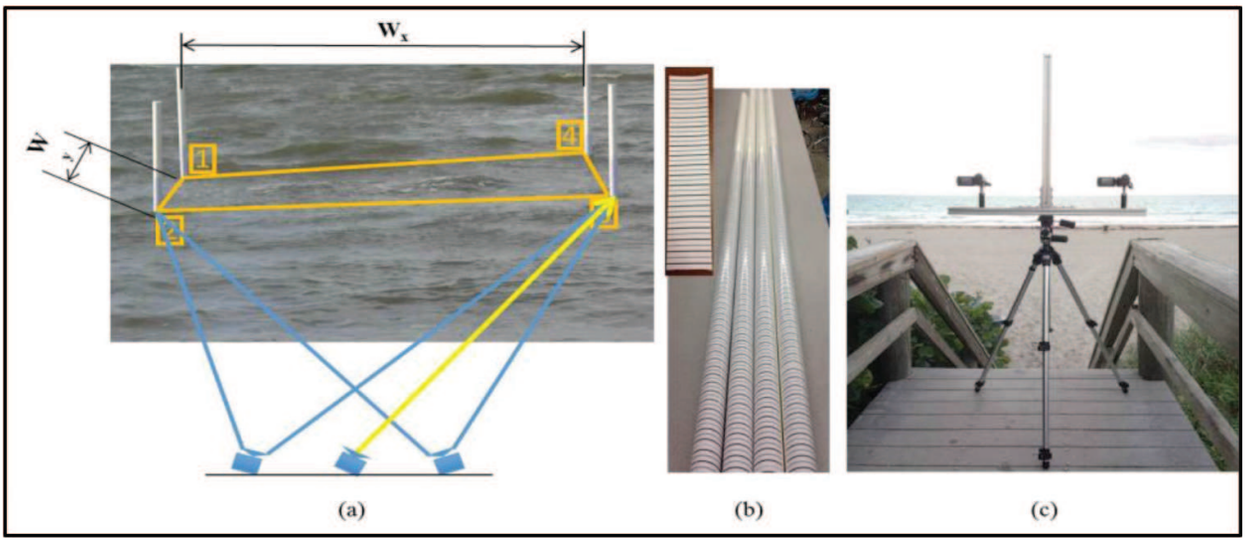

Figure 1. Imaging system deployment and video image of the wave patch (a), staff gauges (b), and example camera deployment platform (c). Target wave patch defined by four staff gauges is 4.5 × 4.5 m (20.25 m^2). Staff gauges were constructed using PVC pipes and striped paper with 0.5 cm line (alternating two colors and thickness) separation. Two video cameras can be used for binocular stereo imaging, and the third camera can be mounted on the vertical bar in the middle or either side in order to conduct a stereo or trinocular imaging of a water patch or zoomed to image staff gauges.

An inverted T-shaped (**Figure 1(c)**) aluminum and steel camera optical mount is used to mount one, two, or three HD cameras. Cameras can be time synchronized, using a known or fixed "digital zoom" mode. During measurement experiments, one camera is focused upon and zoomed (18×) on a staff gauge, and the other two cameras image the entire wave patch and record at 30 Hz or frames per second (fps) (**Figure 2**).

2.2. Image processing

In order to determine the water surface level based on video sequences, three steps are needed as summarized below:

Step 1: Determine the region of interest (ROI)

The water surface level at the staff gauges was clearly observed from the 18× zoomed video frame images. A representative image is shown in **Figure 3(a)**. A ROI was selected to be the area between the top horizontal scale line on the gauge and the bottom margin of the image and was slightly less in width than the actual gauge as defined by the rectangular area in **Figure 3(b)**. A thinner ROI than the actual gauge prevents pixels outside of the staff gauge influencing the results.

Step 2: Average the digital counts within the ROI

Within the ROI, the mean pixel value across each horizontal line is calculated to compress the ROI into a "representative line" shown in **Figure 3(b)**. The average of the three color bands (R, G, B) is calculated in this step as well. The oscillating line in **Figure 3(c)** is the average pixel value of the example frame, and the air-water interface is obvious.

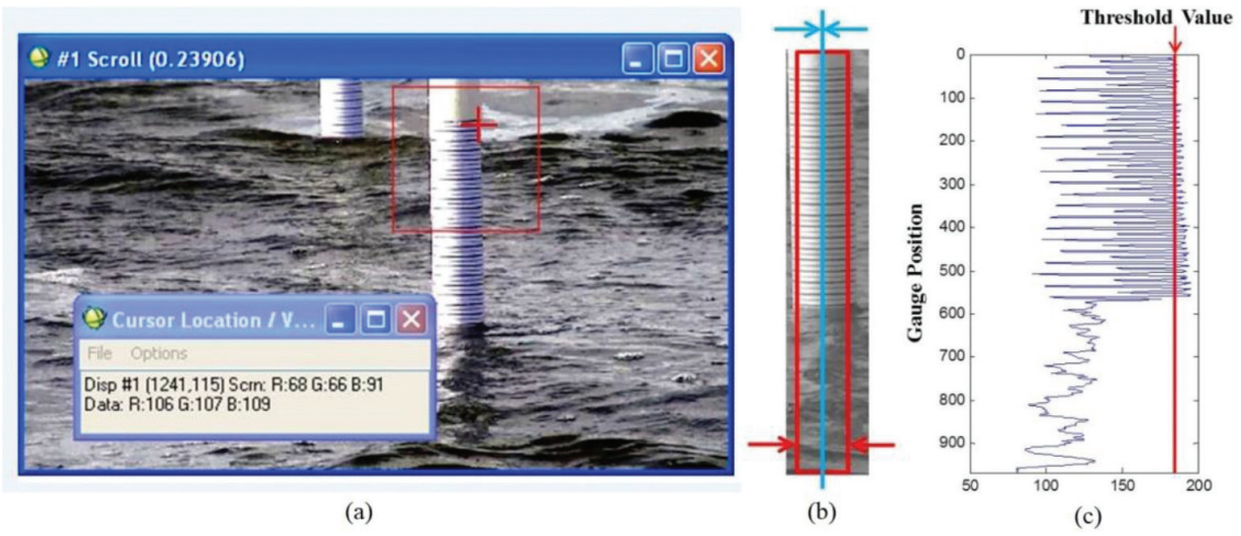

Figure 2. Three steps are used to determine the water surface level from the video. (a) Example of a video frame from the zoomed video (18×). (b) Then, a region of interest (ROI) is defined by a rectangular area, and then a representative line at the center is calculated by averaging the pixel value on each horizontal level. (c) Pixel values along the averaged representative line are shown, and a selected threshold value is selected to locate the interface of water and gauge shown by the solid line.

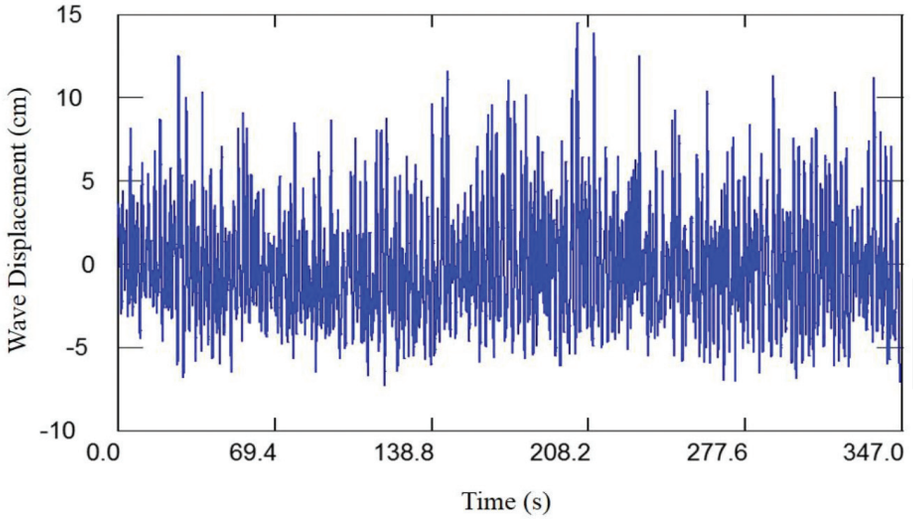

Figure 3. Measured shallow-water surface oscillation series from the video expressed in "wave coordinate." The sequence shown is 347 s with 30 Hz frame rate (10,388 observations). The average water depth during the experiment was 35 cm. The average water surface level during the experiment ranged from 30 cm at the wave troughs and 40 cm at wave crests.

Step 3: Locate the air-water level on the gauge

The shape of the pixel value curve changes dramatically at the interface of water and gauge as shown in **Figure 3(c)**, which is the water surface level. A threshold value is selected in order to automatically locate the interface within each video frame.

The threshold value was determined based on the average of part of the "representative line" (first 500 pixels from the top in the example shown in **Figure 3 (b)**) and it slightly varies from frame to frame. The key is to semiautomatically select a threshold value and apply this value to each frame. The location of the start of values lower than the threshold value is considered as

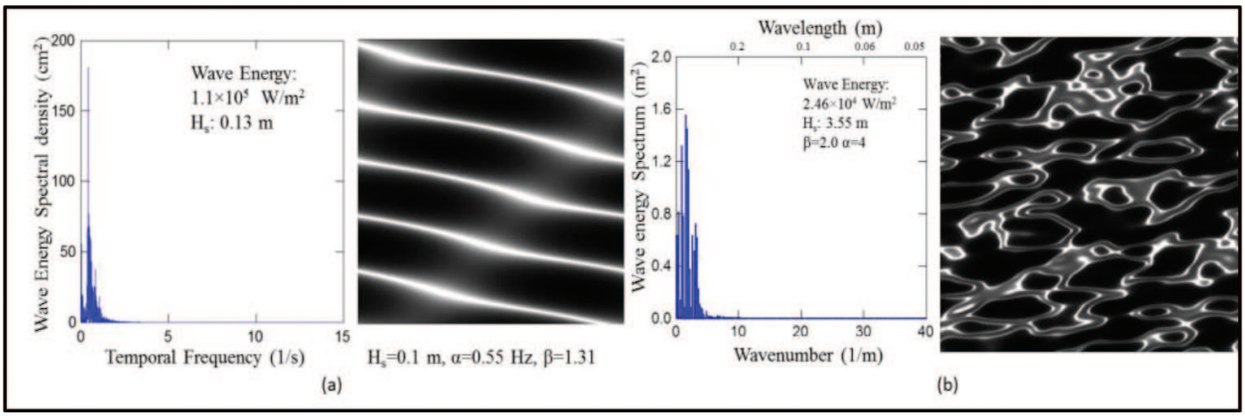

Figure 4. Estimated wave energy spectrum with simulated wave patch (a) and wave energy spectrum with simulated wave patch image using adjusted model coefficients α and β. The peak frequency of the spectrum is 0.39 Hz, and the wave energy in the patch in W/m^2 is 1.1×10^5. The simulated wave patch synthetic images are generated using the estimated wave spectrum from field measurements. The simulated image size is 1024×1024 pixels and represents the 4.5×4.5 m^2 wave patch defined by the staff gauges shown in **Figure 1**. Simulated mean wave height is 7.6 cm, and significant wave height is 0.1 m.

the water surface. **Figure 4** shows the result of 30 Hz time series of the water wave surface oscillations calculated from the example video sequence.

3. Wave spectrum development

A wave energy density spectrum of a wind-driven surface gravity wave patch E can be expressed in units of W/m^2 and is related to the wave height or the variance of the wave displacement, given as $E = \frac{1}{8}\rho g H^2 = \frac{1}{2}\rho g a^2$, where a is the wave displacement and the wave height (H) is twice the wave displacement or $H = 2a$ [1]. Given a measured wave time series, the wave spectrum can be calculated using the fast Fourier transform (FFT) [5]:

$$S(f) = Z_n Z_n^*, \tag{1}$$

where $S(f)$ is the wave spectrum density in the unit of cm^2/Hz, f is temporal frequency in the unit of Hz (1/s), $Z_n = \frac{1}{T}\int_{-T/2}^{T/2} \zeta(t)\exp(i2\pi nft)$ is the Fourier transform of the original signal $\zeta(t)$ (dimensionless), $Z_n^* = \frac{1}{T}\int_{-T/2}^{T/2} \zeta(t)\exp(-i2\pi nft)$ is the conjugate of Z_n (dimensionless), n is the

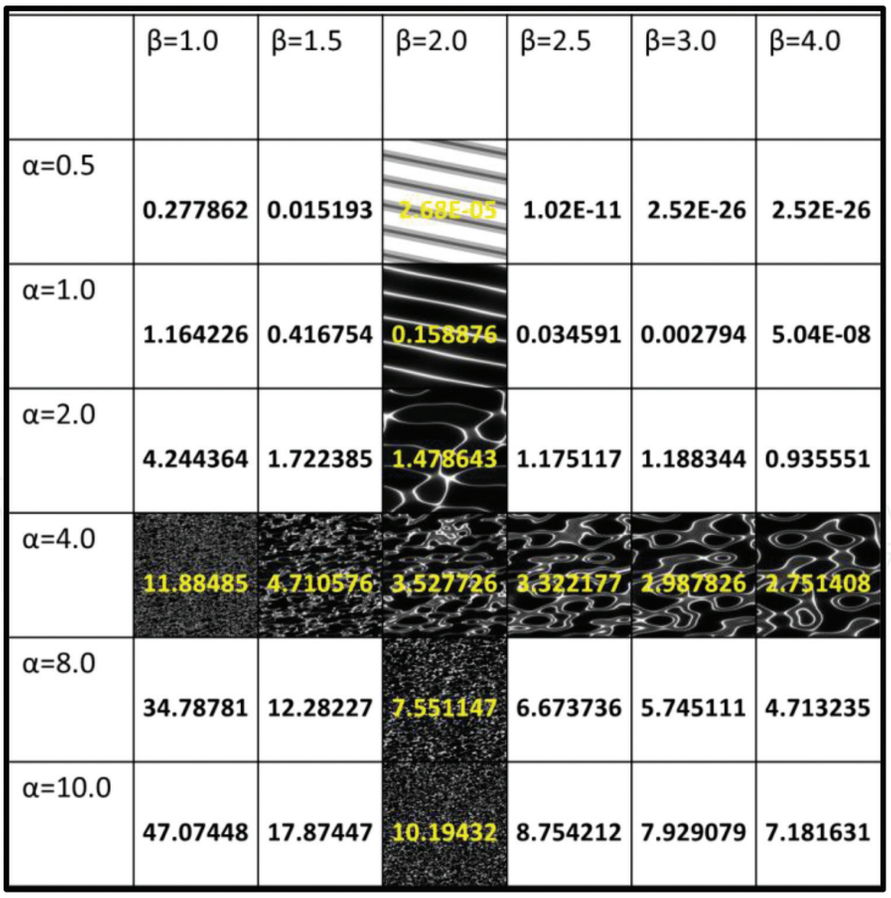

Figure 5. Significant wave height H_s (m) of simulated waves using the wave model (see Eqs. (2) and (3)) parameters α (scale parameter) and β (nondimensional shape parameter) and selected example simulated wave patch synthetic images.

number of the data point in the measured sequence (dimensionless), t is the instant time corresponding to the data point in the unit of second (s), and T is the length of measurement time in the unit of second (s). A two-parameter Weibull distribution function was used as a test model for mathematical expression of the spectrum [2]. The Weibull probability density function (PDF) and cumulative density function (CDF) are given by [9]:

$$\text{PDF} - \text{probability} : (Y) = \left(\frac{\beta}{\alpha^{\beta}}\right) Y^{\beta-1} \exp\left(-\left(\frac{Y}{\alpha}\right)^{\beta}\right) \quad Y > 0, \tag{2}$$

$$\text{CDF} - \text{cumulative} : (Y) = 1 - \exp\left(-\left(\frac{Y}{\alpha}\right)^{\beta}\right) \quad Y > 0, \tag{3}$$

where Y is a variable that follows the Weibull distribution. In this research Y has the unit of 1/s (temporal frequency) or 1/m (wavenumber (spatial frequency); see **Figure 5(a)**), and **Table 1** on x-axis, α = scale parameter has the units of the variable Y, which is 1/s or 1/m, β = non-dimensional shape parameter.

4. Experimental results

4.1. Image-based wave height time series and statistical characteristics

By using the three steps described in Section 2.2, the water surface-level change throughout the video sequence was obtained as shown in **Table 1** and **Figure 4**. Mean wave height of the measured series was 7.9 cm, and significant wave height H_s was 13 cm. The significant wave height H_s is defined as average of the highest one-third of the wave heights [10]. The speed of this wave series extracting process is about two frames per second.

4.2. Wave spectrum, wave energy, and simulation for the Banana River site

The wave spectrum coefficients estimated using the video-based wave series were $\alpha = 0.55$ and $\beta = 1.31$. The calculated wave energy spectrum of the measured wave height time series on temporal frequency domain (Hz) is calculated from Eq. (4):

$$S(\omega) = \left(\frac{\beta}{\alpha^{\beta}}\right) \omega^{\beta-1} \exp\left(-\left(\frac{\omega}{\alpha}\right)^{\beta}\right), \tag{4}$$

where $S(\omega)$ is the wave energy spectral density (m^2/Hz), ω is the temporal frequency (Hz), α = 0.55 is the Weibull scale parameter (Hz), and β = 1.31 is the Weibull shape parameter (dimensionless). The estimated wave spectrum can then be used in the spectral wave patch model [11, 12]. Since the wave simulation program by Bostater et al. [11, 12] was designed to generate a shallow-water gravity wave patch that was independent of time, a dispersion relation was applied to transfer the energy spectrum from temporal frequency domain (Hz) to spatial frequency domain (1/m):

$$\omega(k) = \sqrt{gk\ tanh(kd)}, \tag{5}$$

where $\omega(k)$ is the temporal frequency (Hz), k is the spatial frequency wavenumber (1/m), g is the gravity acceleration (m/s^2), and d is the water depth (m).

The wave energy in the units of W/m^2 can now be calculated using the estimated wave spectrum, based on the area under the spectrum curve [13]:

$$E = \rho g \int S(\omega) d\omega, \tag{6}$$

where E is the wave energy in units of W/m^2 (Joules/s m^2), $S(\omega)$ is the wave energy spectrum in units of m^2, ω is the temporal frequency in units of Hz, $\rho = 1000$ kg/m^3 is the density of the water used in this research, and $g = 9.8$ m/s^2 is the acceleration due to gravity. The discrete approximation of wave energy in this research is calculated by summing the area under the spectral curve:

$$E = \rho g \sum_{0}^{N} S(\omega_n) \Delta\omega_n, \tag{7}$$

where N is the total number of discrete frequencies integral, $S(\omega_n)$ is the magnitude of the energy spectrum at each frequency ωn in units of m^2, and $\Delta\omega_n$ is the discrete frequency interval in units of Hz. A representative shallow-water wind-driven gravity wave can be simulated using the

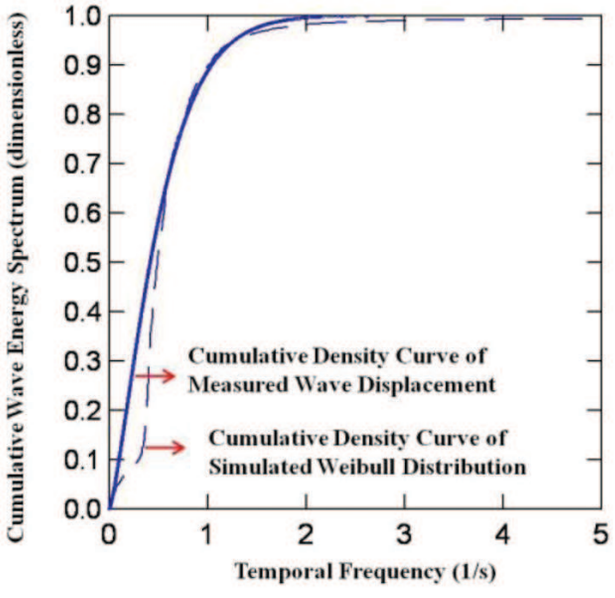

Simulated area in x-y	W_x, W_y	4.5 m² wave patch
Simulated image size	M, N	1024 × 1024 pixels Spatial resolution is 0.004 m/pixel
Gravity acceleration	g	9.8 m/s²
Average water depth	d	0.35 m
Temporal frequency	$\omega(k)$	$\omega(k) = \sqrt{gk\ tanh(kd)}$
Weibull parameters	α, β	$\alpha = 0.55, \beta = 1.31$
Wave energy spectrum	$S(\omega(k))$	$\left(\frac{\beta}{\alpha^{\beta}}\right)\omega(k)^{\beta-1}\ exp\left(-\left(\frac{\omega(k)}{\alpha}\right)^{\beta}\right)$

Table 1. (right) Input equations and parameters for running the wave simulation program (Bostater et al. [11, 12]) for simulating the wave patch shown in **Figure 4** and the measured and simulation distributions (left image). Comparison of the calculated Weibull cumulative curve (solid line) and the cumulative curve of the wave energy spectrum extracted from the measured wave displacements with estimated Weibull parameters of α = 0.55 (Hz) and β = 1.31 (dimensionless) as shown in the table.

http://dx.doi.org/10.5772/intechopen.73042

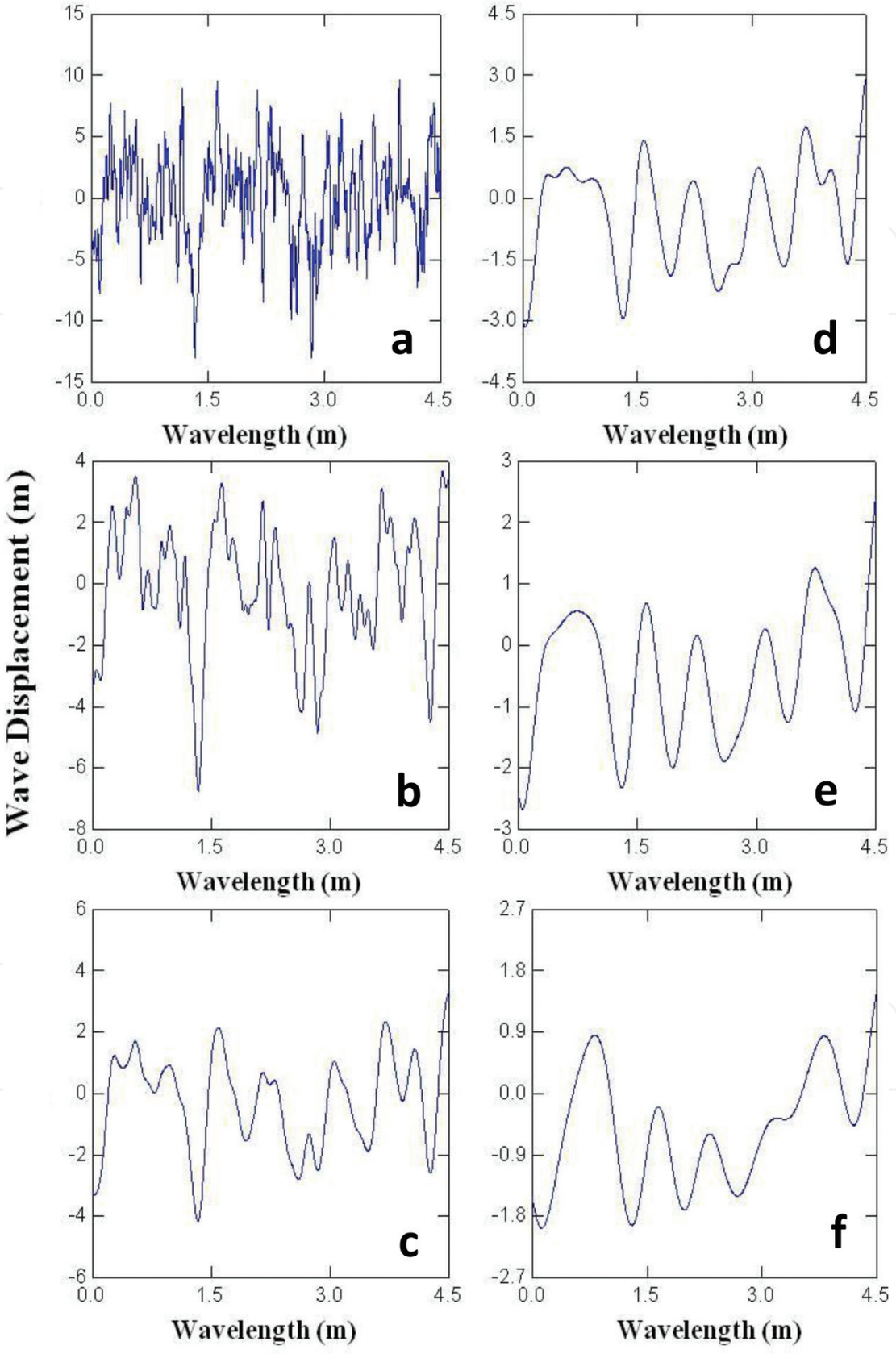

Figure 6. Example shallow-water wave displacement (m) and wavelength (m) sequences (a–f) extracted from synthetic imagery (see **Figure 5**) used to demonstrate the sensitivity of the energy in a simulated wave patch as shown in **Figure 7**. The simulated image results are shown in **Figure 5**.

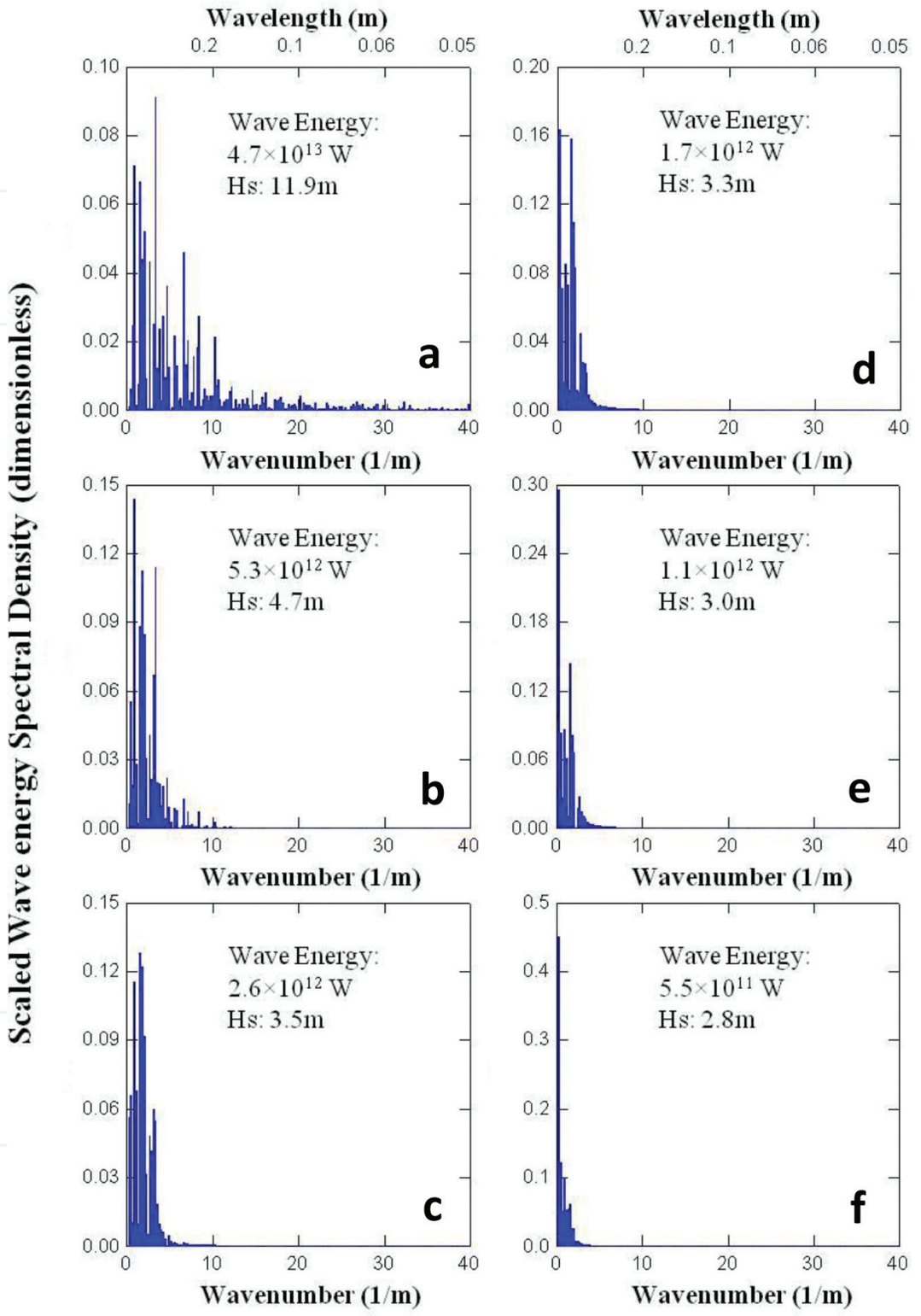

Figure 7. Calculated wave energy in a simulated wave patch for different significant wave heights, wave displacement and wavenumber (spatial frequency) time series (a–f), and synthetic wave patch images shown in **Figure 6**. The representative synthetic mages are shown in **Figure 5**.

estimated wave spectrum from measurements as shown in **Figure 4(a)**. A wave patch simulation model specific for shallow water such as Banana River and Indian River Lagoon was used [8]. The simulated mean wave height is 7.6 cm, and significant wave height is 0.1 m, which is consistent with the video-based measurements. Sensitivity analysis of the simulation model can also be conducted in order to determine the effects of the model coefficients α and β on the simulated wave patches. The results suggest that the model coefficients α and β can affect wave height scale and wave pattern of the simulated wave patches. Therefore, it is reasonable to assume that α and β are related to physical or environmental variables that affect the wave conditions, such as wind speed, wind duration, wind direction, fetch, water depth, bottom slope, etc. When the wave patch model coefficients are adjusted, realistic random water waves are produced as shown in **Figure 4(b)**. The wave energy spectrum (Eq. (4)) can also be introduced or multiplied by a nondimensional scaling coefficient $A = 15$ in this example for sensitivity analysis related to wave patch simulations shown **Figures 4** and **5** (**Table 1**).

A sensitivity analysis of the wave model parameter α (scale parameter) and the β (non-dimensional shape parameter) allows one to clearly see how the water surface wave field would look for different parameter values. The sensitivity simulation results are shown in **Figure 5** with selected wave patch synthetic images for selected model parameters. **Figure 6** shows example wave height displacements, wavenumbers, and significant wave height, and the resulting wave patch energy is simulated wave patches. **Figure 7** shows the associated (a–f) wave energy and significant wave heights obtained from synthetic image model runs. The results demonstrate the utility of making observations, followed by sensitivity analysis and resulting wave patch energy, and associated significant wave heights derived from the synthetic images which are representative measured wind-driven surface gravity wave field patches.

5. Summary

This research developed an imaging methodology to measure wind-driven gravity waves in shallow water using high-definition (HD) video cameras and specially constructed staff gauges. Wave spectrum, wave energy, and significant wave height are estimated from video-based wave height measurement, which can be used to estimate bottom velocity and sediment resuspension. Simulated wave field images are generated using estimated wave spectrum; wave characteristics (significant wave heights) based on the simulation images agree with the in situ video-based measurement protocol and methods described in Section 3 above.

Coefficients α and β in the spectral wave simulation model can affect the wave height and pattern of the simulated wave patches, and they are very likely to be related with some physical and environmental variables. Ongoing research is investigating these variables for these small amplitude water surface waves. The approach developed and described above utilizes the conceptualization shown in **Figure 8**. The energy stored in a surface water gravity wave field drives the sediment resuspension process in the bottom boundary layer and lutocline consisting

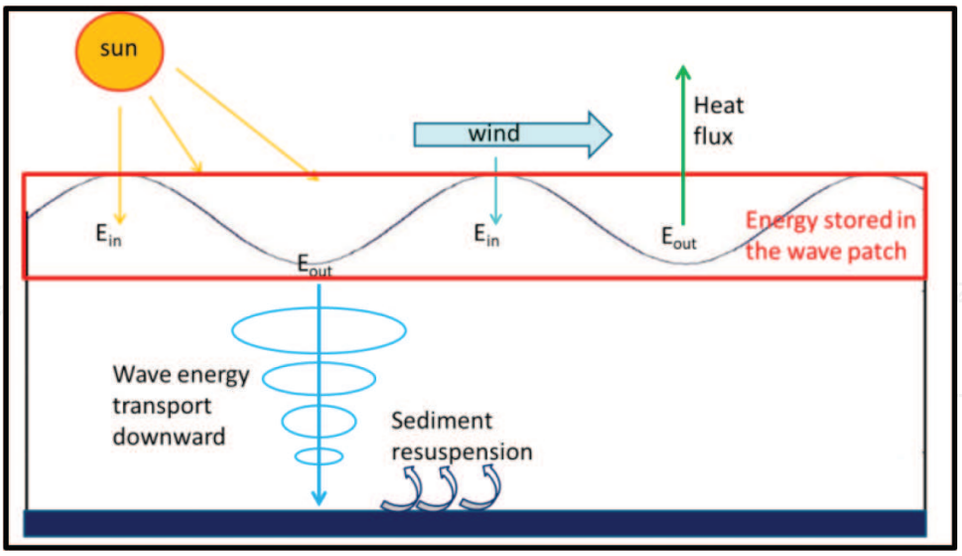

Figure 8. Conceptual model of energy stored in a measured or simulated wave patch and the downward transport of momentum to the bottom boundary layer that can cause resuspension and liquefaction of bottom mud and muck within the lutocline.

of fluid mud and muck. The flowchart shown in **Figure 9** summarizes the protocol and methods described above.

Each time series of water surface displacements is linearly detrended before spectral analysis and calculation of the wind wave energy in the wave field. The mono imaging used in the protocol is the simplest method because water surface elevations can be easily obtained using in situ staff gauges. Algorithms can then be used to calculate wave displacement and wave heights using image processing techniques that analyze each video frame as an instantaneous realization of the water surface elevation or displacement at 0.033 s time intervals. The key for successful mono imaging is the bottom mounted staff gauge used for automatic water surface elevation detection. The staff gauge used in this research was scaled to the appropriate measured wave height field and the gauge and inserted into the bottom sediments.

Simulation of wind-driven water wave patch results shown in **Figure 5** indicates that as α increases, the wave displacement increases and smaller wavelength waves appear on top of the larger waves. The effect of β is just the opposite of α. Increasing β causes decrease in wave displacements with coincident disappearance of smaller waves on top of the larger waves.

The wave energy spectrum graphs (obtained from the synthetic images) shown in **Figures 6** and **7** also provide a visual demonstration of the effect of α and β on wind-driven waves using the Weibull model. Increasing α causes the energy distribution to spread into larger wavenumber in the spatial frequency domain (1/m). This reveals that a simulated wave patch with larger α is consistent with waves with a greater variety of wavelengths. However, increasing β causes the narrowing of the energy distribution to smaller wavenumber (1/m) and suppresses the frequency of larger wavelength waves in a simulated wave patch.

From an energy point of view, wave energy in units of W/m^2 increases with increasing α and decreasing β. The wave energy can be calculated within the simulated wave patch area

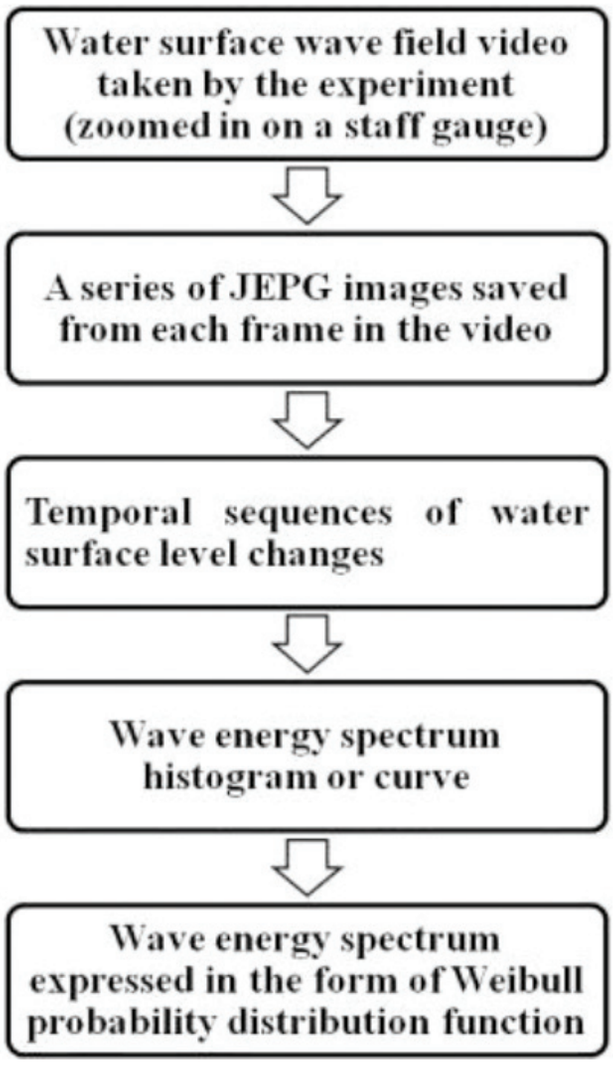

Figure 9. Summary of the general procedures used to extract wind-driven gravity wave energy in a wave patch and resulting wave energy spectrum from measured wind wave videos.

(4.5 × 4.5 m) using the energy distribution from the sum of the variance in the temporal frequency domain [13]. The difference of energy stored in the simulated surface wave patches results in differences in the surface wave heights. In this research, significant wave height was used to represent the simulated surface state.

The significant wave height is defined as the average of the highest one-third of the wave heights [10]. It can be used as a representation of wave height of an observed or simulated wave patch. The tendency of simulated significant wave heights changes with α and β as shown in **Figures 5–7** and suggests that simulated water surfaces are smooth with a small α and large β using the Weibull wave spectrum. A larger α and smaller β tend to produce a rougher surface with more energy. However, considering the shallow-water circumstances of this research, α and β should be limited to a range appropriate to the experimental conditions from field measurements. The authors believe that the techniques, method, and the resulting protocol for the measurement of wind-driven surface water gravity waves described and

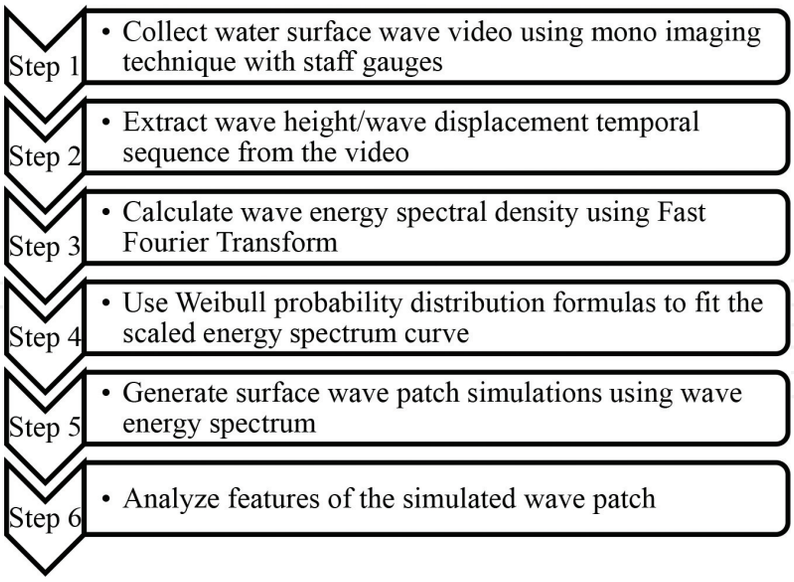

Figure 10. Steps performed to extract wind-driven gravity wave energy and spectra using the protocol methodology described above.

summarized in **Figures 9** and **10** will allow other scientists, engineers, and meteorologists access to an inexpensive and rapidly deployable instrumental approach for shallow waters.

Practical use and applications of water surface video imaging include studying of coastal nearshore processes [14]. The use of fixed sensor video platforms such as bridges, piers, and building which view the littoral zone for water quality constituent determinations has also been demonstrated [15] including the mathematical methods to correct video hyperspectral push broom imagery taken at high oblique angles. Video imaging of bottom features such as seagrasses and sand bottom features has also been demonstrated using practical imaging techniques [16]. The imaging technique described above is being used to assist in assessing moving fluid mud and muck in Indian River Lagoon and Banana River estuarine areas and tributaries [2]. In many shallow-water estuarine regions, wind-driven gravity waves are responsible for resuspension and transport of muds and decaying organic matter within the lutocline [17, 18]. **Figure 11** shows the results of the vertical profile of horizontal mass transport (fluxes) using the water wave video imaging technique in conjunction with simultaneous deployment of a vertical array of six passive Sondes [20] during October 2017. Wind speed during the video wave gauge measurements were 16-17 knots.

Sonde array [20] deployment was 16–17 knots, with east winds in a shallow ≈0.7 m water column and 20–30 cm amplitude wind-driven gravity waves at the location in Banana River near Pineda Causeway [2, 16] near the Atlantic Ocean in Florida (28°12′33.02″N, 80°38′14.72″W). The use of the staff gauge video imaging and Sondes shown in **Figure 11** showed that the shallow-water gravity waves increase the bottom water fine particulate transport or flux of 15,071 g m^{-2} day^{-1} dry weight—nearly 450 times greater than the surface values of 13.1 g m^{-2} day^{-1}. The vertical profile of sediment and particulate mass flux or movement under the waves follows the same profile found in previous studies in tributaries during high flow conditions [19]. The above recent result describes the application of the novel approach to water wave imaging in shallow littoral

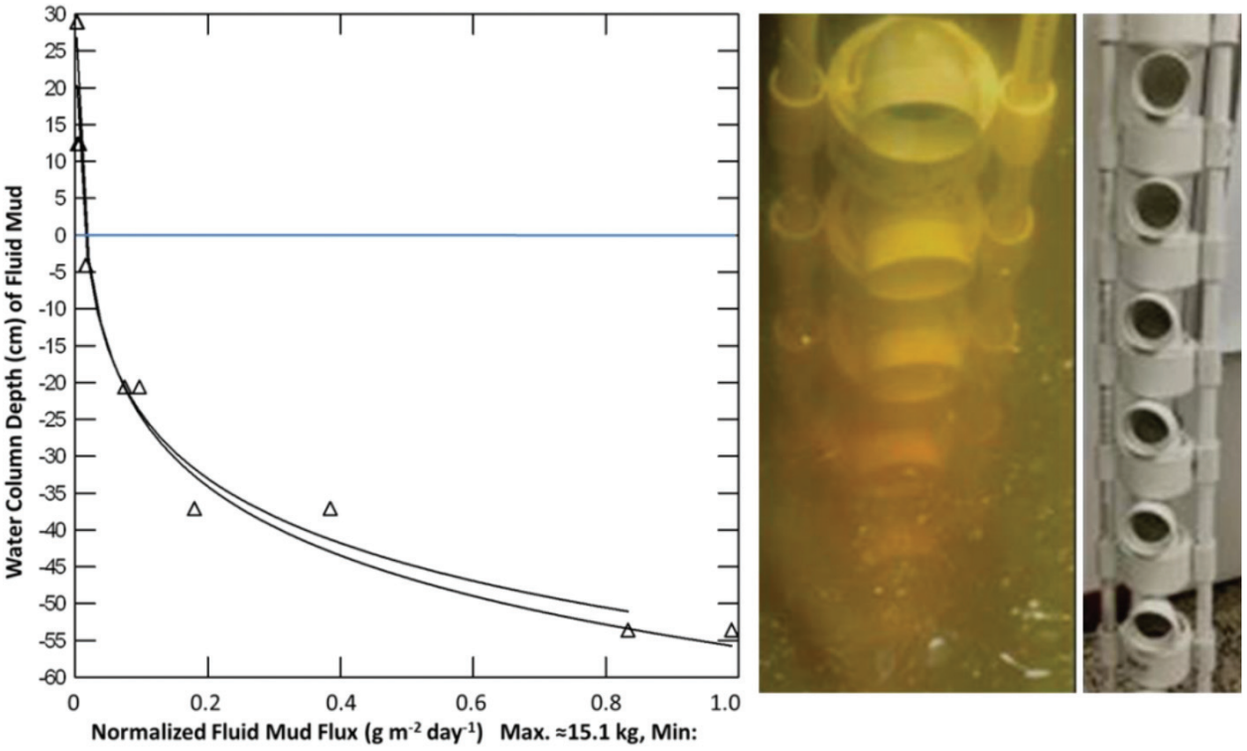

Figure 11. Result (left) from deployment of a vertical array of fluid mud Sondes [20] (right images) in conjunction with video imaging of wind-driven water surface gravity waves (October 2017 (28°12′33.02″N, 80°38′14.72″W)) in a shallow-water littoral zone [2]. The figure demonstrates that water surface gravity waves in shallow coastal areas are responsible for suspending and transporting fluid mud and muck under steady winds of ≈16–17 knots with dry weight mass fluxes (g m^{-2} day^{-1}) at the bottom greater than 450 times the surface transport within surface wave field.

zones. In essence, the novel approach [1] requires no expensive equipment [2], can be easily constructed, and [3] is self-calibrated to video imagery. The method can be used in conjunction with sophisticated wave patch imaging models and when used as a system can be used to improve scientific and engineering understanding of sediment transport due to wind-driven waves. The imaging techniques are currently being used in the field of transportation construction engineering concerned with pile driving rebound imaging and related soil engineering problems.

Acknowledgements

The work presented in this paper has been supported in part by the Northrop Grumman Corporation, the NASA, the Kennedy Space Center, the KB Science, the National Science Foundation, the US-Canadian Fulbright Program, and the US Department of Education, the *FIPSE* and European Union's grant *Atlantis STARS* (Sensing Technology and Robotic Systems) to Florida Institute of Technology, the Budapest University of Technology and Economics (BME), and the Belgium Royal Military Academy, Brussels, in order to support the involvement of students in obtaining international dual US-EU undergraduate engineering degrees.

Author details

Charles R. Bostater Jr*, Bingyu Yang and Tyler Rotkiske

*Address all correspondence to: bostater@fit.edu

Marine Environmental Optics Laboratory and Remote Sensing Center, Ocean Engineering and Sciences, College of Engineering, Florida Institute of Technology, Melbourne, Florida, USA

References

[1] Knauss JA. Introduction to Physical Oceanography. Long Grove, IL: Waveland; 1997

[2] Bostater CR, Yang B. Shallow water surface gravity wave imaging, spectra and their use in shallow water dredging operations. SPIE. 2014;**9240**:92400K-9-92400K-1

[3] Wiberg PL, Sherwood CR. Calculating wave-generated bottom orbital velocities from surface wave parameters. Computers & Geosciences. 2008;**34**:1243-1262

[4] Soulsby RL. Calculating bottom orbital velocity beneath waves. Coastal Engineering. 1987; **11**:371-380

[5] Stewart RH. Introduction to Physical Oceanography. College Station, TX: Texas A&M University; 2004

[6] Benetazzo F, Gallego G, Shih PC, Yezzi A. Offshore stereo measurements of gravity waves. Coastal Engineering. 2012;**64**:127-138

[7] Wanek JM, Wu CH. Automated trinocular stereo imaging system for three-dimensional surface wave measurements. Ocean Engineering. 2006;**33**(5):723-747

[8] Kraus NC. History and Heritage of Coastal Engineering. New York, NY: American Society of Civil Engineers; 1996

[9] Nelson WB. Applied Life Data Analysis. New York, NY: Wiley; 1982

[10] The IAHR Working Group on Wave Generation and Analysis. List of sea-state parameters. Journal of Waterway, Port, Coastal and Ocean Engineering. 1989;**115**(6):793-808

[11] Bostater CR, Chiang G-T, Huddleston L, Gimond M. Synthetic image generation of shallow waters using a parallelized hyperspectral Monte Carlo & analytical radiative transfer model. SPIE. 2003;**5569**:194-208

[12] Bostater CR, Bassetti L. Influence of water waves on hyperspectral remote sensing of subsurface water features. SPIE. 2004;**5569**:194-208

[13] Fréchot J. Realistic simulation of ocean surface using wave spectra. In: Proceedings of the First International Conference on Computer Graphics Theory and Applications (GRAPP), Portugal. 2006. pp. 76-83

[14] Holland KT, Holman RA, Lippmann TC, Stanley J, Plant N. Practical use of video imagery in nearshore oceanographic field studies. IEEE Journal of Oceanic Engineering. 1997; **22**(1):81-92

[15] Bostater CR, Oney TS. Collection and corrections of oblique multiangle hyperspectral bidirectional reflectance imagery of the water surface. SPIE. 2017;**10422**:1042209-1-1042209-22

[16] Bostater CR, Oney TS, Rotkiske T, Aziz S, Morrisette C, Callahan K, Mcallister D. Hyperspectral signatures and WorldView-3 imagery of Indian River Lagoon and Banana River Estuarine Water and bottom types. SPIE. 2017;**10422**:104220E-5-104220E-13

[17] Mehta A, Lee A, Li Y. Fluid Mud and Water Waves: A Brief Review of Processes and Simple Modeling Approaches. US Army Corps of Engineers, CR DRP-94-4. 1994. 79 pp

[18] McAnally W et al. Management of fluid mud in estuaries, bays, and lakes, II: Present state of understanding on character and behavior. Journal of Hydraulic Engineering, ASCE. 2007;**133**:23-38

[19] Vanoni VA, editor. Sedimentation Engineering. American Society of Civil Engineering, ASCE Hydraulic Division Task Committee. 1975. p. 745. ISBN: 0-87262-001-8

[20] Bostater C, Rotkiske T, Oney T, Obot E. "Design and Operation of Sonde Arrays to Measure Fluid Mud in the Marine Environment", Proceedings of ISOPE. 2017. pp. 1511-1514. ISBN: 978-1-880653-97-5

IntechOpen